AGU PUBLICATIONS

JGR

Journal of Geophysical Research: Planets

RESEARCH ARTICLE
10.1002/2016JE005146

Key Points:
- Unprecedented 3-D resolved convective layer of Venusian cloud layer and induced gravity waves
- Convection layer organized as polygonal closed cells of several kilometers wide
- Strong impact of the global circulation on the convection and its variability

Correspondence to:
M. Lefèvre,
maxence.lefevre@lmd.jussieu.fr

Citation:
Lefèvre, M., A. Spiga, and S. Lebonnois (2017), Three-dimensional turbulence-resolving modeling of the Venusian cloud layer and induced gravity waves, *J. Geophys. Res. Planets*, *122*, 134–149, doi:10.1002/2016JE005146.

Received 29 JUL 2016
Accepted 16 NOV 2016
Accepted article online 23 NOV 2016
Published online 20 JAN 2017

Three-dimensional turbulence-resolving modeling of the Venusian cloud layer and induced gravity waves

Maxence Lefèvre[1], Aymeric Spiga[1], and Sébastien Lebonnois[1]

[1] Laboratoire de Météorologie Dynamique, UMR CNRS 8539, Institut Pierre-Simon Laplace, Centre National de la Recherche Scientifique, Sorbonne Universités, UPMC Univ Paris 06, Paris, France

Abstract The impact of the cloud convective layer of the atmosphere of Venus on the global circulation remains unclear. The recent observations of gravity waves at the top of the cloud by the Venus Express mission provided some answers. These waves are not resolved at the scale of global circulation models (GCM); therefore, we developed an unprecedented 3-D turbulence-resolving large-eddy simulations (LES) Venusian model using the Weather Research and Forecast terrestrial model. The forcing consists of three different heating rates: two radiative ones for solar and infrared and one associated with the adiabatic cooling/warming of the global circulation. The rates are extracted from the Laboratoire de Météorlogie Dynamique Venus GCM using two different cloud models. Thus, we are able to characterize the convection and associated gravity waves in function of latitude and local time. To assess the impact of the global circulation on the convective layer, we used rates from a 1-D radiative-convective model. The resolved layer, taking place between 1.0×10^5 and 3.8×10^4 Pa (48–53 km), is organized as polygonal closed cells of about 10 km wide with vertical wind of several meters per second. The convection emits gravity waves both above and below the convective layer leading to temperature perturbations of several tenths of kelvin with vertical wavelength between 1 and 3 km and horizontal wavelength from 1 to 10 km. The thickness of the convective layer and the amplitudes of waves are consistent with observations, though slightly underestimated. The global dynamics heating greatly modify the convective layer.

1. Introduction

Venus hosts a global sulfuric acid cloud layer between 45 and 70 km which has been investigated in detail by the Venus Express mission. One of the main questions that remains unclear about the dynamics of the Venusian atmosphere, and its interaction with the photochemistry is how this convective cloud layer mixes momentum, heat, and chemical species and generates gravity waves. Gravity waves emitted by the convection have been proposed to promote a significant contribution to the maintenance of the super-rotation [*Hou and Farrell*, 1987]. However, these waves develop from regional to local scales and cannot be resolved by global circulation models (GCM) developed so far to study Venus' atmospheric dynamics. Before a subgrid-scale parametrization of those convectively induced waves can be developed in existing GCMs, small-scale ("mesoscale") modeling is needed to explore the dynamics of convection and waves in the Venusian cloud layer.

The strong dynamical activity in the cloud layer has been known for a long time. The Mariner 10 mission [*Belton et al.*, 1976] and the Pioneer Venus spacecraft [*Rossow et al.*, 1980] used the UV marker to follow patterns at the top of the cloud layer and evidenced cellular features with sizes between 200 and 1000 km. The Pioneer Venus probes investigated the dynamics of the Venus atmosphere: a region of neutral stability between 50 and 55 km was detected [*Seiff et al.*, 1980] and small-scale waves with vertical wavelengths of about 7 km were observed [*Seiff et al.*, 1980; *Counselman et al.*, 1980]. The VEGA missions sent two balloons in the convective layer [*Sagdeev et al.*, 1986], which floated at approximately 54 km at 7°N and 7°S. The balloons measured vertical winds ranging between −3.5 and 2 m s^{-1} inside the convective layer [*Linkin et al.*, 1986] and encountered convective cells with an estimated width from several hundred meters to tens of kilometers [*Kerzhanovich et al.*, 1986].

The Venus Express [*Svedhem et al.*, 2007] mission has been able to investigate the dynamics of the atmosphere and detect small-scale waves at the top of the cloud layer with the help of the Venus Monitoring Camera (VMC) [*Piccialli et al.*, 2014], the Visible and InfraRed Thermal Imaging Spectrometer (VIRTIS) [*Peralta et al.*, 2008], and the Venus Radio science device (VeRa) [*Tellmann et al.*, 2009, 2012]. A strong variability of the convective layer with latitude was observed [*Tellmann et al.*, 2009] with a vertical extent between 49 and 59 km. The Venus Express instruments also measured the wavelengths of the waves which range between about 2 and 3.5 km along the vertical [*Tellmann et al.*, 2012] and from 2 km to hundreds of kilometers in the horizontal [*Peralta et al.*, 2008; *Piccialli et al.*, 2014]. The observations also provided the spatial variability of the waves, which are mainly observed at high latitudes, with a potential link with the topography [*Bertaux et al.*, 2016]. The long duration of the Venus Express mission, from 2006 to 2014, enabled a precise study of the top of the cloud over several Venus years [*Markiewicz et al.*, 2007; *Titov et al.*, 2012; *Hueso et al.*, 2015]. The observations made with VMC illustrated the different morphologies of the cloud on the dayside, hinting at distinct dynamical regimes. At low latitudes, mottled dark clouds dominate, suggesting convective activity. Around 50° latitude, the clouds tend to be streaky, suggesting a horizontal laminar flow. At higher latitude, the clouds are bright and almost featureless.

Several numerical models have been developed to investigate the dynamics of the convection layer and the associated gravity waves. The pioneering models proposed in the 1980s [*Schubert and Walterscheid*, 1984; *Young et al.*, 1987] and the 1990s [*Leroy and Ingersoll*, 1995] were one-dimensional models focusing on the vertical wave propagation in an idealized Venusian atmosphere. Starting from the 2000s, two-dimensional mesoscale models [*Baker et al.*, 1998, 2000a, 2000b; *McGouldrick and Toon*, 2008; *Imamura et al.*, 2014] were developed to resolve the convective layer and the associated gravity waves.

The first two-dimensional model of the Venusian cloud layer was built by *Baker et al.* [1998, 1999, 2000a, 2000b]. The model focuses on the convective layer between 47 and 55 km [*Baker et al.*, 1998, 1999], and the interaction of this layer with another convective layer between 18 and 30 km, either without [*Baker et al.*, 2000a] or with [*Baker et al.*, 2000b] wind shear. The forcing is similar in both studies, a solar heating model at subsolar point. *Baker et al.* [1998] predicted the development between 47 and 55 km of alternating updrafts and downdrafts over 15–30 km in the horizontal, with vertical wind increasing with the solar flux from 2 to 7 m s^{-1}, and the emission below and above the cloud layer of gravity waves with horizontal wavelengths of 5–30 km. *Baker et al.* [2000a] discussed the emission of gravity waves in the stable layer between the two convective layers. The results obtained are two strong convective layers with maximum vertical wind of about 15 m s^{-1}. *Baker et al.* [2000b] suggested that the presence of a wind shear may create interaction between the two convective layers, resulting in the emission of stronger gravity waves.

The modeling study by *McGouldrick and Toon* [2008] focuses on microphysical processes in the cloud layer. The dynamical forcing is produced by a vertical wind parametrization designed to mimic the effect of convective motions resolved by *Baker et al.* [2000b]. With this model, *McGouldrick and Toon* [2008] obtained gravity wave perturbations of several kelvins, consistent with the VeRa observations [*Tellmann et al.*, 2012], and associated variation of the optical depth.

The most recent two-dimensional model by *Imamura et al.* [2014] is forced with solar heating rates based on in situ measurements and infrared heating rates globally averaged over the planet. The main result of the *Imamura et al.* [2014] modeling study is the inverse insolation dependence of the convection. The convection in Venus' cloud layer is stronger at high latitude, which is consistent with the VeRa observations [*Tellmann et al.*, 2012], and at night.

Despite past achievements, two-dimensional models have not been able, by design, to address the three-dimensional organization of the convective layer and, in particular, the size, and shape of observed convective cells. Moreover, the move toward three-dimensional modeling for the Venusian convective cloud layer ensures a more complete prediction of the gravity waves emitted by convective motions. This has been recently explored by *Yamamoto* [2014] through idealized three-dimensional numerical experiments using prescribed lapse rate of the potential temperature and turbulent thermal flux.

In this paper, we propose unprecedented three-dimensional turbulence-resolving simulations for the Venusian convective cloud layer and the associated gravity waves. Our model is the first to combine three-dimensional dynamical integrations with realistic solar and infrared radiative forcing. This allows us to improve on *Yamamoto* [2014] and revisit the questions raised by this work on the variability of convective

activity and emitted gravity waves with local time and latitude. Another novel aspect of our model of the Venus' cloud layer is the inclusion of the thermal forcing induced by the large-scale circulation in addition to the radiative forcing.

Our paper is organized as follows. The model is described in section 2. In section 3, we describe the results on convective motions and gravity waves from a reference simulation. We then explore in section 4 the variability of this dynamical activity with latitude and local time. The impact of the global circulation, and the adopted cloud model, on the convective activity is discussed in section 5. Our conclusions are summarized in section 6.

2. Large-Eddy Simulations for Venus

2.1. Dynamical Integrations

Our three-dimensional simulations are based on the Weather Research and Forecast (WRF) terrestrial model [*Skamarock and Klemp*, 2008]. The WRF dynamical core integrates the fully compressible nonhydrostatic Navier-Stokes equations on a chosen area of the planet. The mass, momentum, and entropy conservation are ensured by an explicitly conservative flux-form formulation of the fundamental equations, based on mass-coupled meteorological variables (winds and potential temperature). To simulate the convective motions, and associated gravity waves, in the Venusian cloud layer, we use the WRF dynamical core as a turbulence-resolving model in so-called large-eddy simulations (LES): the mesh spacing is set to a few hundred meters to resolve the largest turbulent eddies (i.e., plumes) responsible for the majority of energy transport and mixing processes by buoyant convection [*Lilly*, 1962; *Sullivan and Patton*, 2011]. The remainder of turbulent mixing exerted by small, unresolved, eddies is accounted for by a subgrid-scale "prognostic Turbulent Kinetic Energy" closure [*Deardorff*, 1972], similar to what is done in WRF LES for the Earth [*Moeng et al.*, 2007] and Mars [*Spiga et al.*, 2010].

We focus in this study on both the Venusian cloud layer and the gravity waves emitted above this convective layer, so we chose domain settings and resolutions compliant with existing two-dimensional studies [*Baker et al.*, 1998, 2000a, 2000b; *McGouldrick and Toon*, 2008; *Imamura et al.*, 2014]. The vertical domain ranges from 40 to 70 km. The chosen horizontal resolution is 200 m, and the vertical resolution follows an exponential law with a mean value of 145 m. We set 181 grid points in the three spatial dimensions, so the domain extent is $36 \times 36 \times 30$ km. This choice of spatial resolution requires a temporal resolution of 1.2 s, as a trade-off between numerical stability and computational efficiency and small enough to provide high temporal resolution over the lifetime of a convective cell. The horizontal boundary conditions are periodical, and at the top of the domain a free relaxation condition sets vertical velocity to zero. In this study, no background wind shear is imposed (i.e., no atmospheric superrotation).

2.2. Radiative and Dynamical Forcing

Our Venus LES model couples the WRF dynamical integrations with an off-line radiative and (large-scale) dynamical forcing based on heating rates extracted from simulations with the Laboratoire de Météorologie Dynamique (LMD) Venus GCM [*Lebonnois et al.*, 2010]. We use the most up-to-date LMD Venus GCM run which reached superrotation (similar to the ones described in *Lebonnois et al.* [2016]). The solar flux scheme is based on *Crisp* [1986]. The IR transfer [*Lebonnois et al.*, 2015] is based on *Eymet et al.* [2009], in an updated version that uses the cloud model of *Haus et al.*, 2013 [2013, 2014]. Figure 1 details the three distinct heating rates coupled with our dynamical integrations: two radiative ones for short wave (solar) and long wave (IR) and the adiabatic cooling/warming due to the global dynamics of the atmosphere (mainly the Hadley cell, *Lebonnois et al.* [2016]). Heating rates in this paper are expressed in kelvin per Earth day (K/Ed) to compare with previous works. Those heating rates are applied at each dynamical time steps in our model and remain constant throughout the LES integrations.

Figure 1 shows that the behavior of each heating rate is different. The solar heating rate is strictly positive and increases up to 7.0×10^3 Pa, decreases, and then increases again above 3.0×10^3 Pa. The IR radiative and dynamics rates add up to mirror the solar rate. These two rates generally decrease with the altitude up to 7.0×10^3 Pa, increase, and then decrease above 3.0×10^3 Pa. For the IR radiative rate there are also two areas of increase below 7.0×10^3 Pa: above (4.0×10^4 Pa) and below (1.0×10^5 Pa) the convective layer. The IR rate significantly increases and even become positive below the convective layer. The increase below the convective layer has no variability with latitude nor local time, while the one above the convective layer has a strong variability with the position on the planet. The dynamical heating rate decrease with altitude is caused

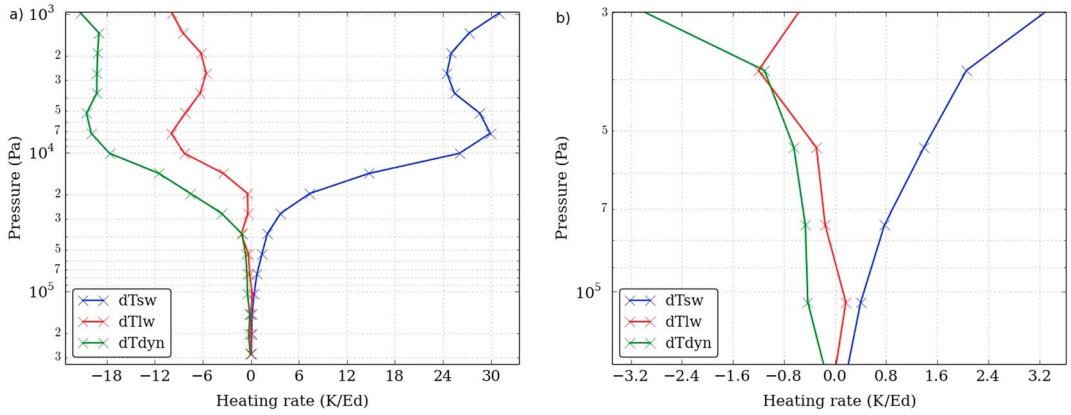

Figure 1. The three types of heating rates in kelvin per Earth day (K/Ed) extracted from LMD Venus GCM and used for the forcing: (a) over the whole vertical extent and (b) more specifically in the convective layer. Conditions: equator, LT 12 h (noon). Symbols indicate the vertical resolution of the GCM. dTsw stands for the short-wave rate (solar), dTlw for the long-wave rate (IR), and dTdyn for the global dynamics rate.

by the rising branch of the Hadley cell and associated adiabatic cooling (this is described in further details in section 4.2 and Figure 16). We could therefore expect a significant variability of the convective motions with latitude.

The initial state of the LES model is interpolated from a temperature profile predicted by the same GCM run as the one from which heating rates are extracted. The WRF dynamical core uses potential temperature instead of temperature. In Venusian conditions, caution must be exerted when converting the initial profile and the heating rates from temperature to potential temperature. Following *Lebonnois et al.* [2010], we use a specific heat capacity C_p varying with temperature following the formulation

$$C_p(T) = C_{p_0}\left[\frac{T}{T_0}\right]^{\nu} \tag{1}$$

with $C_{p_0} = 1000.0$ J kg^{-1} K^{-1}, $T_0 = 460.0$ K and $\nu = 0.35$. The potential temperature formulation then can be written

$$\theta^{\nu} = T^{\nu} + \nu T_0^{\nu} \ln\left[\frac{P_{\text{reff}}}{P}\right]^{\kappa_0} \tag{2}$$

with $P_{\text{reff}} = 92.0 \times 10^6$ Pa and $\kappa_0 = R/C_{p_0}$, and the static stability S can be written

$$S = \frac{\mathrm{d}T}{\mathrm{d}z} + \frac{g}{C_p(T)} \tag{3}$$

where $\mathrm{d}T/\mathrm{d}z$ is the variation of temperature with altitude and g the acceleration of gravity. The value of the Brunt-Väisälä frequency N is computed from $N^2 = \frac{g}{T}S$. Figure 2 shows the initial state of the domain (vertical static stability profile). The convective layer is clearly seen in the profile as a neutral stability layer extending (for this configuration: equatorial location and local time noon) from 5.0 to 7.0×10^4 Pa.

Our simulations are run long enough so that the combination of radiative and (large-scale) dynamical heating rates act to destabilize the initial atmospheric profile and to cause convective instability, thereby triggering vertical motions resolved by our LES dynamical integrations which act to mix heat and momentum in the cloud layer. After several Venusian hours, the system reaches a steady state. Hence, the mixed profile obtained in the cloud layer stems from the plumes resolved by LES integrations, in complete independence from the initial mixed profile from the GCM (which was generated by a subgrid-scale parameterization in this model).

3. Simulated Convection and Gravity Waves

We will now focus on a Venus LES run using heating rates for the equator at noon (LT 12 h) to study first the convective behavior, then the induced gravity waves.

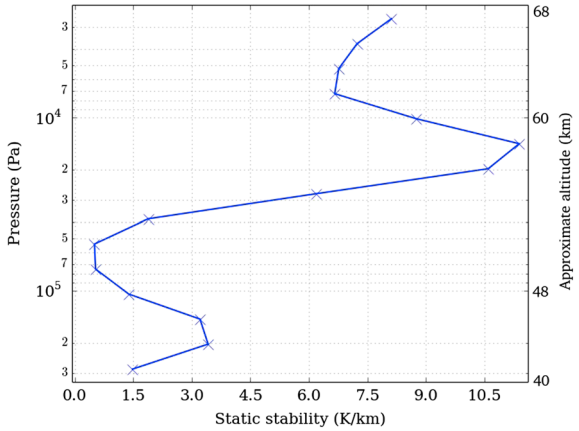

Figure 2. Initial static stability (K/km) vertical profile extracted from the LMD Venus GCM, for the equator at noon. Symbols indicates the vertical resolution of the GCM.

3.1. The Convective Layer

Figure 3 represents the average static stability and the average potential temperature vertical profiles. Averages are computed the following way: when the simulation has reached the steady state, the average profile is calculated by taking the average at each vertical level over the entire horizontal domain. The perturbation of a quantity X is $X' = X - \overline{X}$ with $\overline{X}$ the average vertical profile (or value at the vertical level of interest) of the quantity.

The zero value of the static stability and the constant value of the potential temperature indicates that the convection takes place between 6.0×10^4 and 3.8×10^4 Pa (50.1 and 53.3 km) with low static stability down to 1.0×10^5 Pa (48 km). In the radio occultation measurements of VeRa [*Tellmann et al.*, 2009] the convective layer at the equator was located between approximately 49 and 59 km. The bottom of the resolved convective layer is consistent in altitude with the observations, although the convection is thinner. The values of the static stability in the model, up to 15 K/km, are also weaker than in the observations (25 K/km). The small-scale structures above and below the convective layer are inherited from the vertical linear interpolation from the GCM vertical resolution, from the vertical cloud structures and also from the resolved motions.

Figure 4 shows two snapshots of the convective motions: a vertical cross section in the middle of the domain and a horizontal cross section in the middle of the convective layer, at 4.7×10^4 Pa. Values of vertical wind weaker than observations are predicted by the model: between −1.6 and 1.2 m s^{-1} against −3.5 to 2 m s^{-1} for the measurements made by the VEGA balloons [*Linkin et al.*, 1986]. Figure 4b delivers information about the organization of the convection. The convective layer develops as closed hexagonal-like type of cells, i.e., with broad updrafts in the center of the cells and narrow downdrafts at the edge. This indicates that radiative cooling in the middle cloud drives the convection [*Agee et al.*, 1973] and leads to downdrafts being stronger than

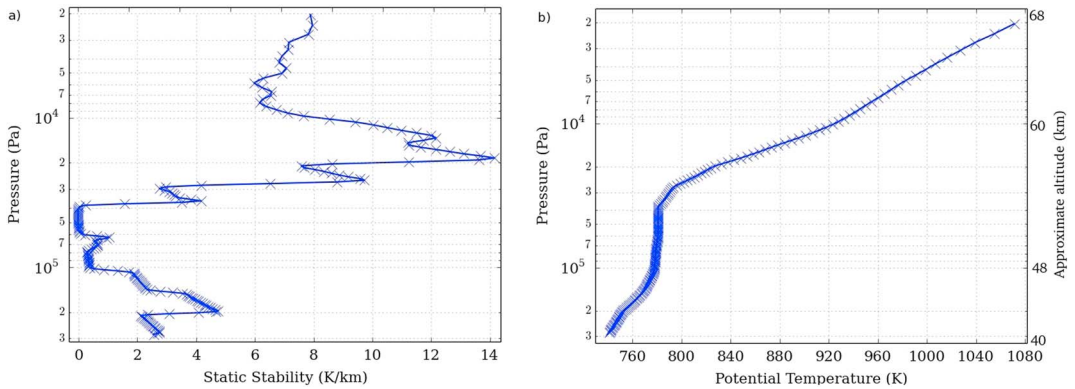

Figure 3. (a) Average static stability (K/km) vertical profile and (b) average potential temperature (K) vertical profile, for equator, noon. Here and after the symbols indicate the vertical resolution of the LES model, except when it is indicated.

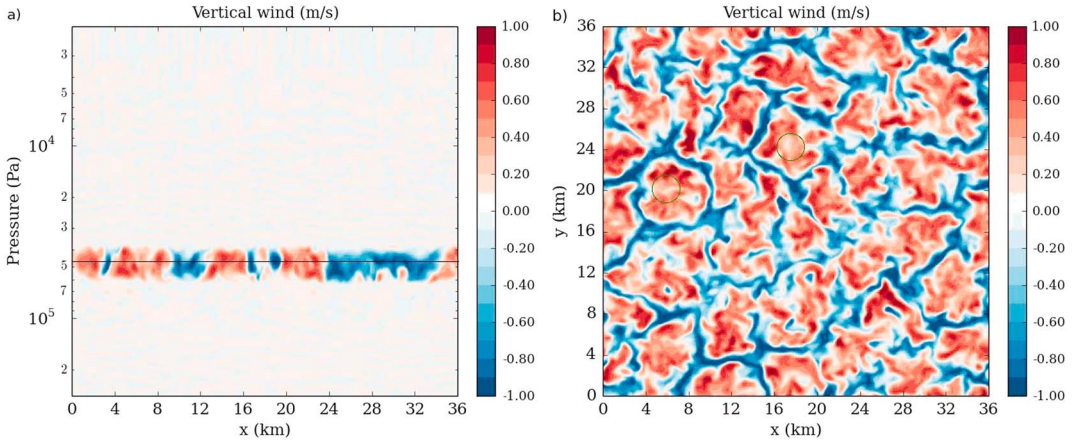

Figure 4. Snapshots of the convective vertical motions: (a) vertical cross section at $y = 18$ km and (b) horizontal cross section at 4.7×10^4 Pa of the vertical wind (m s^{-1}), for Equator, noon. The black line in Figure 4a represents the location of the horizontal cross section in Figure 4b. The green circles represent location discussed in the text.

updrafts. These cells are about 6 km wide, which is consistent with, but, again slightly lower than the VEGA measurements [*Kerzhanovich et al.*, 1986], whereas the downdrafts are only a couple kilometers thick. The aspect ratio of the cells $\frac{\text{width}}{\text{height}}$ is then approximately 3, while on the Earth the value for closed cell is between 3 and 28 due to much wider cells [*Atkinson and Zhang*, 1996].

The vertical eddy heat flux defined as $C_p \rho \overline{w'\theta'}$ (in W m^{-2}, with C_p the specific heat calculated from equation (3), ρ the density calculated with the ideal gas law, θ' the potential temperature perturbation, and w' the vertical wind perturbation) is shown in Figure 5. The heating rate (in kelvin per Earth day) associated with resolved convective motions is, to first order, equal to the negative of the vertical gradient of $\overline{w'\theta'}$. The flux is increasing in the bottom half of the convective layer (from 6.0×10^4 to approximately 5.0×10^4 Pa) and decreasing in the top half. Thus, convection acts to cool down the bottom half of the convective layer and warm up the top half. This heat transport, in conditions where $\overline{\theta'w'} > 0$, is exerted mostly by warm updrafts ($\theta' > 0$ and $w' > 0$) and cold downdrafts ($\theta' < 0$ and $w' < 0$). By analogy with planetary boundary layer (PBL) convection on the Earth and Mars, we could define this core layer of convective motions as the mixing layer. This mixing layer is capped by a thin layer where $\overline{w'\theta'}$ is both increasing (i.e., convection cools down this layer) and negative (i.e., heat transport exerted by cold updrafts and warm downdrafts): the action of updrafts thus dominates in this layer, which we identify as an updraft-induced entrainment layer by analogy with terrestrial and Martian PBL convection (an interpretation that differs from *Baker et al.* [1998]). The mixing layer is also overlying a thin layer where $\overline{\theta'w'}$ is both decreasing (i.e., convection warms up this layer) and negative (i.e., heat transport exerted by warm updrafts and cold downdrafts): the action of downdrafts thus dominates in this layer, which we identify as a downdraft-induced entrainment layer (which has no counterpart in terrestrial and Martian PBL,

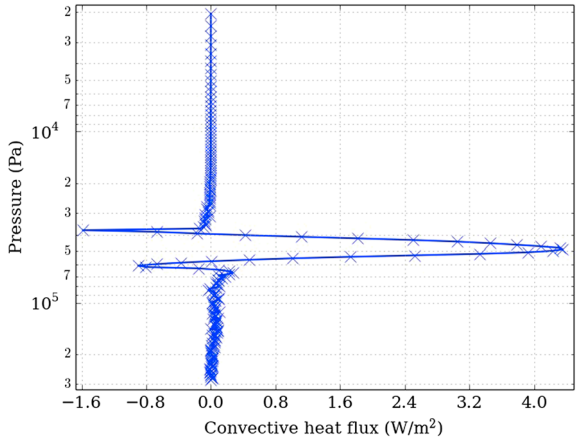

Figure 5. Vertical profile of the turbulent heat flux (W m^{-2}), for Equator, noon.

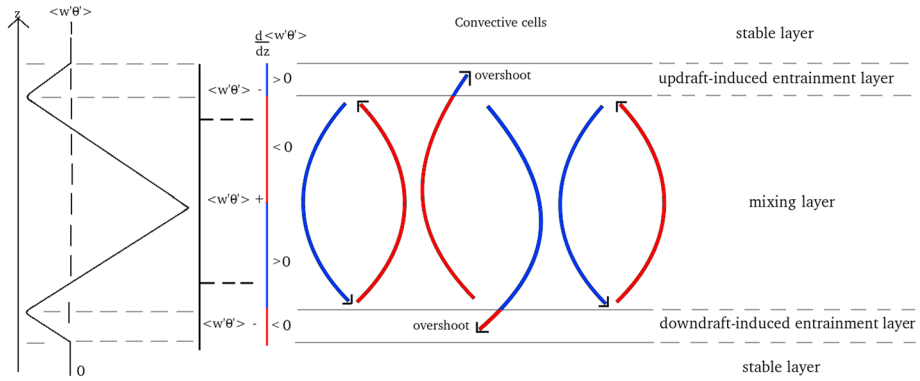

Figure 6. Schematic representation of the link between the convective cells with associated convection heat flux and layers. (left) The vertical profile of $\overline{w'\theta'}$ with its sign. Next to it is the sign of the vertical gradient of $\overline{w'\theta'}$ with color representing warming for red and cooling for blue. Then is represented several plumes with color representing warm ($\theta' > 0$) for red and cool for blue ($\theta' < 0$).

an interpretation similar to *Baker et al.* [1998] and *Imamura et al.* [2014] although, in contrast to *Baker et al.* [1998], we also name this layer an entrainment layer). Thus, according to our simulations, the convective cloud layer on Venus is made of a mixing layer that is underlain and overlain by two entrainment layers, the one above where the action of updraft overshoots dominate and the one below where the action of downdraft overshoots dominate (making the two sides propitious to the emission of gravity waves). Figure 6 sums up the link between the convection cells and associated convective heat flux. This results from the convection being forced from below by net warming and above by net cooling, as a result of the infrared, visible, and large-scale dynamical contributions detailed in Figure 1.

3.2. The Induced Gravity Waves

Here and after we use the Cartesian system as coordinate system with the vertical axis as z axis, and the two horizontal axis as x axis and y axis.

Figure 7 displays a snapshot of a vertical cross section of the temperature perturbation at $y = 18$ km and an instantaneous vertical profile of the temperature perturbation at $x = 18$ km. The induced gravity waves are visible as alternating positive and negative perturbations of temperature. The gravity waves are emitted both below and above the convective layer. The perturbations are between −0.13 and 0.16 K, while VeRa measured the temperature perturbations between −1.7 and 1.7 K at 19.6° of latitude [*Tellmann et al.*, 2012]. The gravity waves obtained are weak compared with the observations but as is mentioned above, this is directly linked to the modeled convective layer being weaker than observed.

The peak-to-peak amplitude of temperature perturbations above the convective layer is quite constant up to 2.0×10^4 Pa, while it strongly decreases above this level (at approximately 10^4 Pa, around 59 km, the inten-

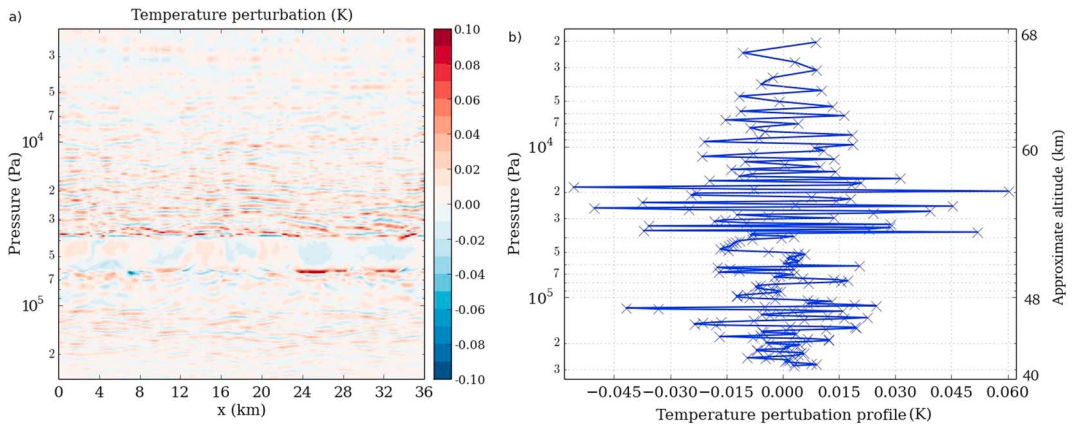

Figure 7. Snapshots of the gravity waves: (a) temperature perturbation (K) vertical cross section and (b) instantaneous vertical profile at the center ($x = 18$ km and $y = 18$ km) of the domain, for equator, noon.

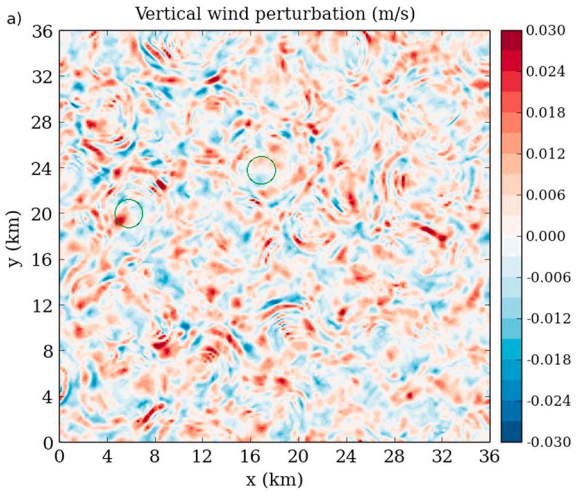

Figure 8. Snapshot of the gravity waves: the horizontal cross section of the vertical wind (m s^{-1}) perturbation at 3.0×10^4 Pa, for equator, noon. The green circles represent location discussed in the text.

sity of the waves becomes too weak and no wavefront is discernible). A similar decrease is observed in the radio occultation carried out using the Magellan [*Hinson and Jenkins*, 1995] spacecraft and the Venus Express [*Tellmann et al.*, 2012] missions. At first glance, this phenomenon is counterintuitive, since the decrease of density with altitude usually causes an increase in the amplitude of the waves [*Frits and Alexander*, 2003]. However, in a very similar way to the static stability (Figure 3a), above the convective layer the Brunt-Väisälä frequency decreases between 2.0×10^4 Pa and 5.0×10^3 Pa (this decrease may be linked to the radiative damping of the atmosphere [*Hinson and Jenkins*, 1995]). Such variation with altitude of the Brunt-Väisälä frequency could imply a variation with altitude of the energy of the waves [*VanZandt and Fritts*, 1989], namely, when the frequency decreases the energy decreases. The fact that the amplitude of the waves decreases with altitude would indicate that the impact of the decrease of the Brunt-Väisälä frequency is stronger than the impact of the decrease of the density. This is further suggested by the emitted gravity waves being high-frequency gravity waves (see below), which makes them particularly sensitive to changes in background Brunt-Väisälä frequency.

In the horizontal plane, the wavefront of the gravity waves is circular as illustrated in Figure 8 with the vertical wind perturbation, 1 km above the convection at 3.0×10^4 Pa (see, e.g., the green circles at $x = 6$ km and $y = 20$ km or $x = 18$ km and $y = 24$ km). These structures are correlated with the position of the updrafts (see the green circles in Figure 4): when the plumes reach the top of the convective layer, they encounter and perturb the stable layer above. This leads to the emission of gravity waves [*Fovell et al.*, 1992], which propagate vertically and horizontally with no preferred axis (i.e., with circular wave fronts, note that the effect of a background wind shear on the propagation of those waves will be investigated in another study). Therefore, stronger plumes lead to stronger waves.

To characterize the waves, we use a continuous wavelet transform with the Morlet wavelet defined in *Torrence and Compo* [1998] (Python software by Evgeniya Predybaylo, available in this URL http://paos.colorado.edu/research/wavelets). In Figure 9, we obtain through this wavelet transform that the horizontal wavelength ranges from 1 to 5 km. The multiplicity of the wavelengths suggests possible interference between the waves. The values of the wavelengths are consistent with the observations, between 2 and 30 km for VMC [*Piccialli et al.*, 2014], but still on the lower side of the spectrum. This can be attributed to the weak convection, but also to the size of the domain: with a wider one, larger wavelengths should be able to develop. We applied the same methodology for vertical wavelengths, it ranges between 1 and almost 3 km below the convective layer, the same order of magnitude of the VeRa observations, between 2 and 3.5 km [*Tellmann et al.*, 2012].

Using the horizontal and vertical wavelengths of the gravity waves, the intrinsic angular frequency $\hat{\omega}$ (the angular frequency ω with respect to the background wind) can be estimated. Since the background wind shear is set to zero, the intrinsic frequency is equal to the frequency. Given that the Coriolis parameter, $f = 2\Omega\sin(\phi)$, is negligible because of the weak rotation Ω of the solid body, and considering that the square

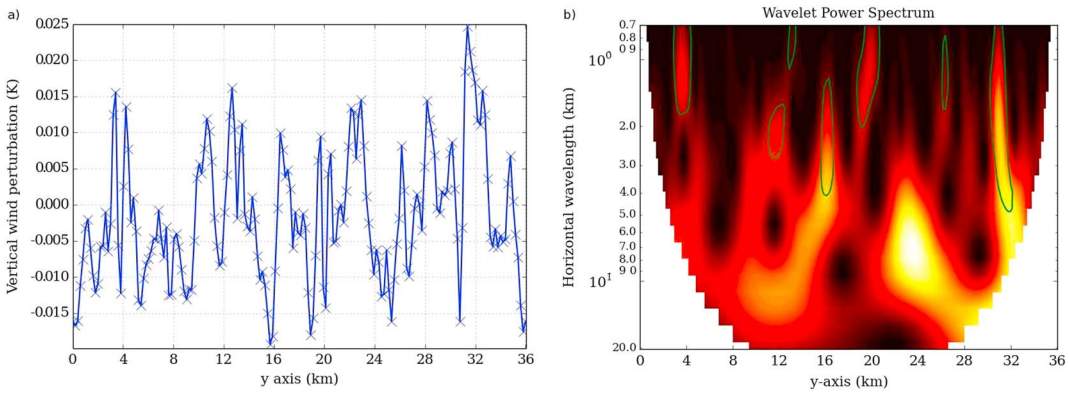

Figure 9. (a) Vertical wind perturbations (m s^{-1}) cross section at 3.0×10^4 Pa and $x = 18$ km and (b) the associated wavelet power spectrum, for equator, noon. The areas circled in green are the areas with at least 95% of confidence level.

of the vertical wave number $m^2 \gg 1/4H^2$ with H the Venus scale height (equals to 7 km in the cloud), the dispersion relation [*Frits and Alexander*, 2003] then reads

$$\omega^2 = \frac{N^2\left(k^2+l^2\right)}{k^2+l^2+m^2} = \frac{N^2\left(k_h^2\right)}{k_h^2+m^2} = N^2\cos^2\alpha \tag{4}$$

where N is the Brunt-Väisälä frequency, k, l, and m, respectively, are the wave number in the x axis, y axis, and z axis, and α is the angle between the line of constant phase and the vertical axis. From the circular wavefront we can assume that k and l are equal and so we define k_h as the horizontal wave number equal to $\sqrt{k^2+l^2}$. The order of magnitude of N^2 above the convective layer (10^{-4} s^{-2}) is consistent with observations by the Pioneer Venus probes [*Gierasch et al.*, 1997]. With a vertical wavelength of 1.5 km and horizontal wavelengths of 1 and 5 km, the angular frequencies are 9×10^{-3} and 3.9×10^{-3} s^{-1}, i.e., the high-frequency regime close to N. The associated angle α are 25.23° and 67.01°.

With the same assumptions as the ones made for the dispersion relation, the group velocity (c_{gh}, c_{gz}) defined as $\partial\omega/\partial k$ simplifies as

$$(c_{\mathrm{gh}}, c_{\mathrm{gh}}) = (\overline{u_h}, 0) + \frac{Nm}{k_h^2+m^2}\frac{(m,-k_h)}{\left(k_h^2+m^2\right)^{1/2}} = \frac{Nm}{k_h^2+m^2}\frac{(m,-k_h)}{\left(k_h^2+m^2\right)^{1/2}} \tag{5}$$

with c_{gh} and c_{gh}, respectively, the horizontal group velocity and the vertical group velocity. The group velocities with the different horizontal wave numbers vary from −0.39 to −0.79 m s^{-1} for the vertical component and from 0.18 to 1.8 m s^{-1} for the horizontal component. The horizontal phase velocity, defined as $\frac{\omega}{k}$, ranges from 1.43 to 3.1 m s^{-1} for horizontal wavelengths of 1 and 5 km. These values are the same order of magnitude (from 5 to 10 m s^{-1}) that the VeRa observations [*Tellmann et al.*, 2012] and the ones in *Baker et al.* [2000a]. The measured meridional wind reaches several meters per second [*Hueso et al.*, 2012; *Khatuntsev et al.*, 2013]; thus, the wave packets propagating in the right meridional direction would reach critical level and eventually break. It appears less probable that this would occur in the zonal direction given the amplitude of super-rotating winds [*Sánchez-Lavega et al.*, 2008]. A full LES study of the waves with a background wind shear is necessary and is considered as future work.

To summarize, the model predicts a convective layer too thin, though with realistic vertical winds, and provides insight on the cellular organization of the convection. The amplitude of the gravity waves is impacted by the weak convection; they are of lower amplitude than the observations and with wavelengths in the order of magnitude of the smallest observed.

4. Variability With Local Time and Latitude

Observations of the gravity waves on Venus [*Peralta et al.*, 2008; *Tellmann et al.*, 2012; *Piccialli et al.*, 2014] showed a strong variability with latitude (with a preference for higher latitudes). In the VeRa observations [*Tellmann et al.*, 2009], the convective layer is thicker at high latitude but exhibits no clear variability with local time, which is at odds with the model predictions of *Imamura et al.* [2014]. In what follows, we discuss the variability of the modeled convective layer with local time and latitude.

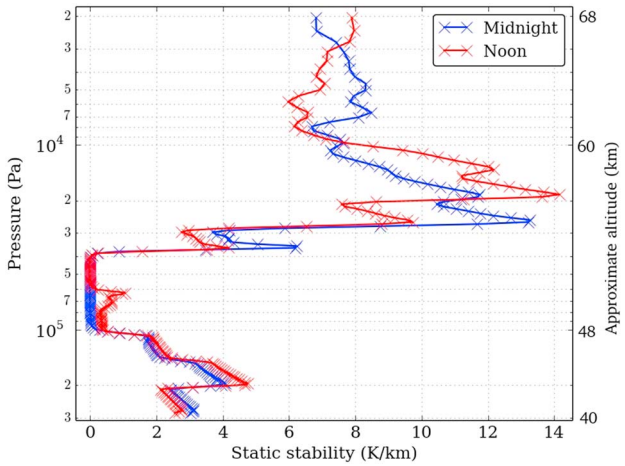

Figure 10. Comparison of the average static stability vertical profile (K/km) at the equator, for noon (LT 12 h) and midnight (LT 00 h).

4.1. Variability With Local Time

Figure 10 shows the average static stability at the equator compared between noon and midnight. The convection is thicker at midnight; it extends from 1.0×10^5 to 3.8×10^4 Pa (from 48 to 53.3 km). At midnight (Figure 11) the vertical wind ranges from −2.9 at 2.2 m.s^{-1} in the middle of the convective layer. The cells are also larger, with typical width of 15 km. With a vertical extent of 5 km and, the aspect ratio is equal to 3, very similar to the one at noon. The temperature perturbations are also stronger (Figure 12a) at midnight compared at noon, typical values are between −0.35 and 0.5 K with circular wavefront (Figure 12b). Horizontal wavelengths are similar to the noon simulation, except for some very localized areas with horizontal wavelength of almost 10 km, while vertical wavelengths reach 3 km.

The equator showing a stronger convection at midnight is not observed: the VeRa profiles exhibit very low variability with local time. However, the behavior of our model is consistent with the simulations of *Imamura et al.* [2014]. The stronger convection at midnight is interpreted as a stabilization of the convection by the solar heating of the cloud top. The IR heating rates are similar in the convective layer (between 1.0×10^5 and 4.0×10^4 Pa) for the two configurations, but the heating rates associated with the global circulation are different (Figure 13): negative at noon, no clear trend at midnight. At noon the dynamical heating rate compensates the solar rate, which results in a weaker convection than at midnight.

At 60° of latitude, the convection at noon and midnight are very similar (Figure 14). The convective layers extend from 5.8×10^4 Pa and 5.5×10^4 Pa for, respectively, noon and midnight to both 3.8×10^4 Pa. The

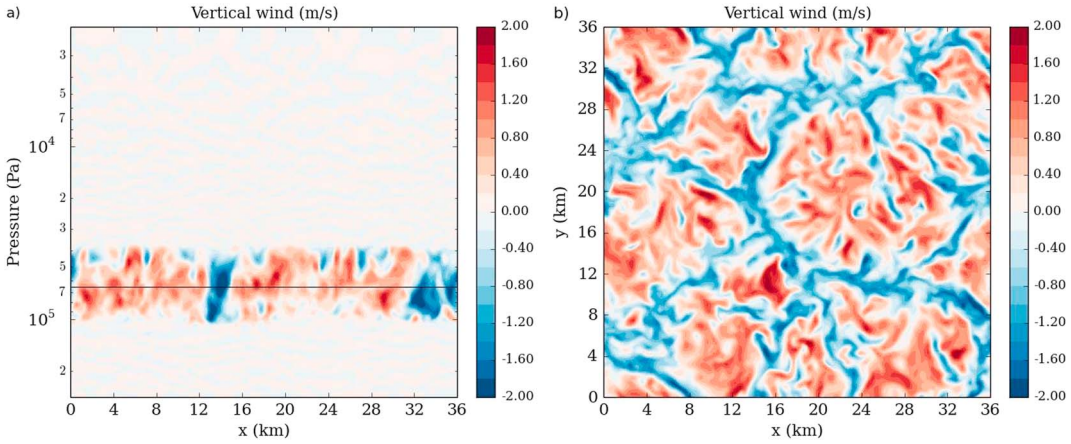

Figure 11. Snapshots of the convective vertical motions: (a) vertical cross section and (b) horizontal cross section at 6.4×10^4 Pa of the vertical wind (m s^{-1}), for the equator, midnight. The black line in Figure 11a represents the location of the horizontal cross section in Figure 11b.

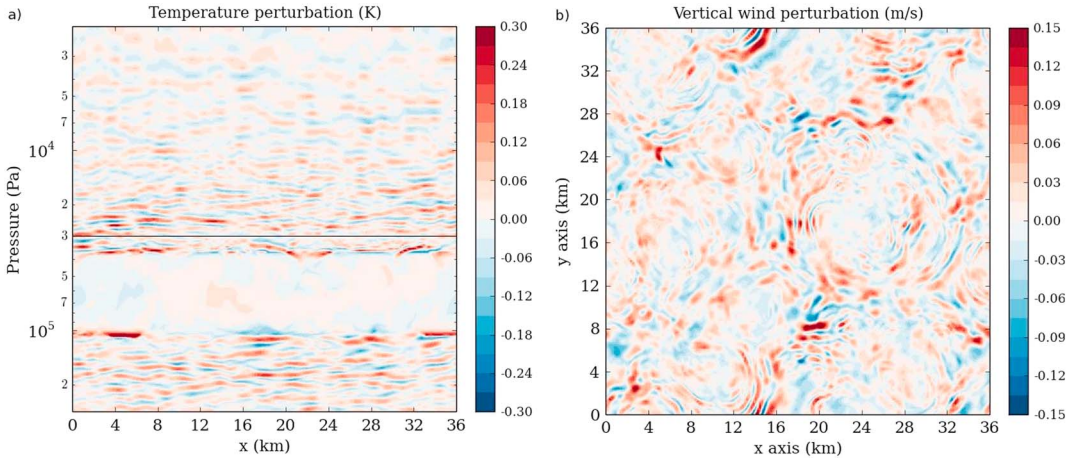

Figure 12. Snapshots of the gravity waves: (a) temperature perturbation (K) vertical cross section and (b) horizontal cross section of the vertical wind perturbation (m s^{-1}) at 3.0×10^4 Pa, for equator, midnight. The black line in Figure 12a represents the location of the horizontal cross section in Figure 12b.

vertical winds are between −1.5 and 1.2 m s^{-1} at noon and between −1.0 and 0.75 m s^{-1} at midnight. The temperature perturbations at noon are about ± 0.15 K against ± 0.10 K at midnight. The wavelengths of the associated waves are similar to the equator noon case. The IR heating rates are extremely similar, while the heating rates associated with the global circulation have two different behaviors (Figure 13). The dynamical heating rate at noon oscillates between positive and negative values below 2.8×10^4 Pa while being 1 order of magnitude less than the radiative heating rates at the top of the cloud. Conversely, the dynamical heating rate at midnight has a behavior similar to the solar heating rate at noon: positive and increasing with altitude in the same order of magnitude. Thus, at night, the adiabatic warming by the global circulation compensates the absence of solar heating, resulting in the convective layer at midnight and noon being of similar extent.

4.2. Variability With Latitude

At noon (Figure 15) there is very low meridional variability in the vertical extent of the convective layer between the equator and 60° of latitude. This behavior is not consistent neither with the VeRa profiles nor with the model of *Imamura et al.* [2014] which both exhibit a significant variability with latitude. Nevertheless, the predictions of our model are consistent with the imposed radiative and large-scale dynamical heating rates. In the convective layer region, the IR heating rate is exactly similar in our model for both latitudes. The solar heating rate is approximately 3 times stronger at the equator. The dynamics heating rate (see Figure 13) at the equator is negative and about the same order as the IR heating rate and follow a behavior symmetrical to the solar heating rate. At 60° the dynamics heating rate is weak, about 1 order of magnitude lower.

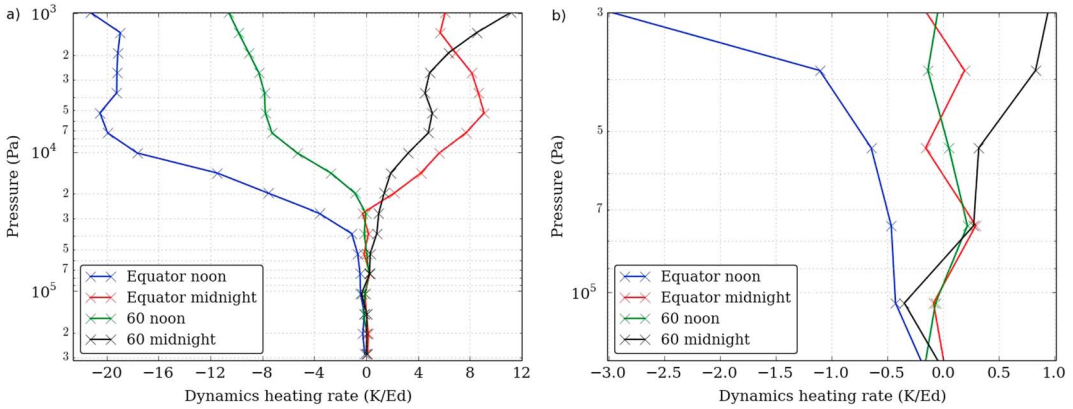

Figure 13. Global dynamics heating rates in Kelvin per Earth day (K/Ed) extracted from the LMD Venus GCM: (a) over the whole LES vertical domain and (b) in the convective layer. The four profiles represent the four configurations studied. The symbols represent here the vertical resolution of the GCM.

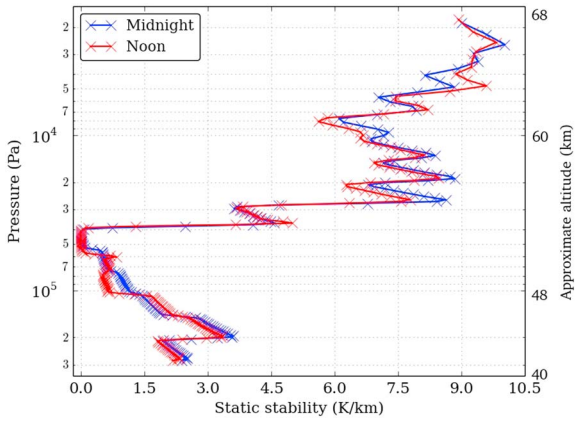

Figure 14. Comparison of the average static stability vertical (K/km) profile at 60° latitude, for noon and midnight.

Thus, at the equator the solar rate and the global circulation rate compensate each other, which results in a weak convection; at 60° the situation is similar (although with weaker rates), which results in a similarly weak convection than that close to the equator. Our model also predicts that contrary to noon at midnight, the convection is stronger at the equator. This is due to a strong heating rate of the global dynamics at 60° that compensates the IR heating rate, while at the equator the weak global dynamics heating rate leads to a thick convective layer.

Figure 16 illustrates the link between the convective layer and the global circulation of the GCM. The global dynamics is clearly different between day and night. At 60° of latitude, the convective layer is within a descending branch at midnight and within a rising branch at noon. In contrast, at the equator, it is within the uprising branch of the Hadley cell both at noon and midnight. This is in agreement with the imposed dynamical heating rates (Figure 13), showing an adiabatic warming at 60° at midnight, and an adiabatic cooling at the equator at noon.

These discrepancies between observations and our model deserve further comments. The global geographical coverage of the VeRa retrievals [*Tellmann et al.*, 2009] would have allowed to detect variations with local time. The absence of observations of gravity waves at low latitude (inferior to 40°), due to a lack of brightness contrast [*Piccialli et al.*, 2014], could be something very interesting to investigate further with the ongoing Akatsuki mission or the future missions. The simplicity of the forcing used, completely dependant of the GCM simulations and especially on the low vertical resolution of the convective layer heating rates may lead to some approximations on the heating rates. The temporal and horizontal homogeneity of the forcing could as well have a significant impact on the convective layer: with such spatial resolution the radiative-photochemical-dynamical feedbacks could be very important. We are therefore currently developing a mesoscale model coupled to the full radiative scheme to better resolve this kind of mechanism.

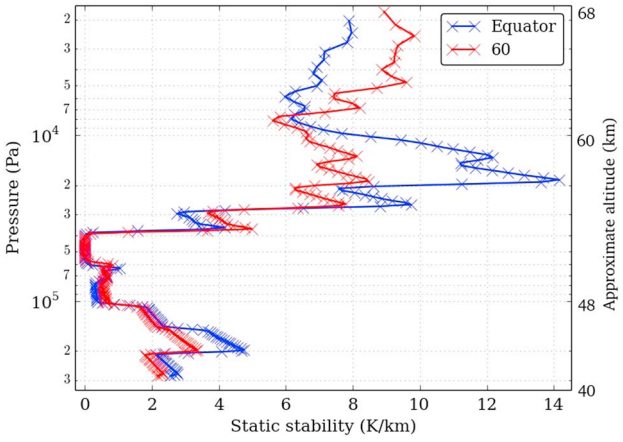

Figure 15. Comparison of the average static stability (K/km) vertical profile at noon, between equator and 60° latitude.

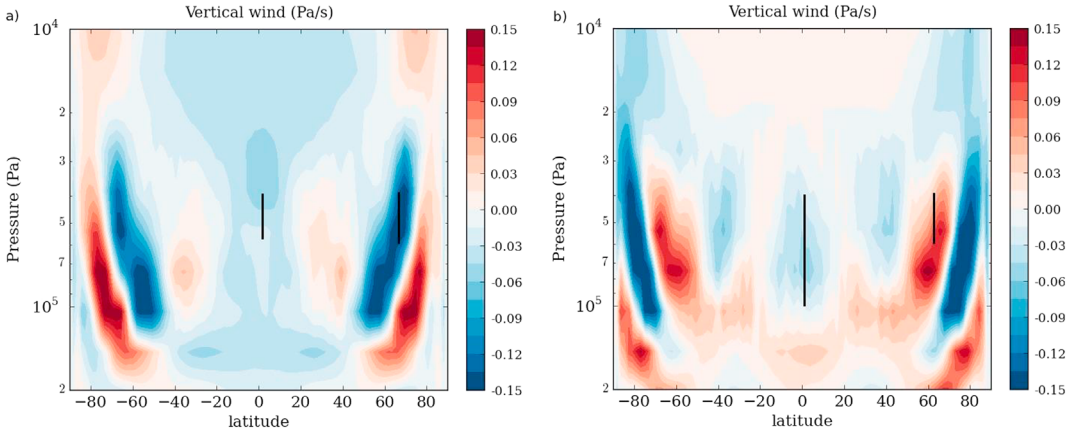

Figure 16. LMD Venus GCM vertical wind: (a) at noon and (b) midnight in the cloud convective layer altitudes. The black lines represent the convective layer of the four spatial configuration. The units is in Pa/s; therefore, positive value means negative (downward) vertical wind in m s^{-1} and conversely.

Furthermore, the GCM uses a cloud model uniform in latitude; this may have an impact on the variability with latitude. The variability of the cloud model with latitude will be implemented in future studies.

5. Impact of the Global Circulation and the Cloud Model

5.1. Global Circulation Dynamics

As it is described above, the global circulation plays an important role on the convective layer by warming and cooling the atmosphere. To assess in a more quantitative fashion the impact of this circulation, we carried out Venus LES with heating rates calculated from a one-dimensional version of the LMD Venus GCM. In other words, the heating rates correspond to a purely radiative-convective model devoid of large-scale dynamics: the solar heating rate is similar to our reference Venus LES and the IR heating rates too (up to the top of the convective layer), while the dynamical heating rate is zero.

Figure 17 is a comparison of the static stability at the equator at midnight between the reference Venus LES and the one using forcing from one-dimensional radiative-convective computations. The convection is thicker when the large-scale dynamical heating rate is not included: it extends from 1.1×10^5 to 2.5×10^4 Pa (47.5 to 56.4 km) with vertical wind between −4.7 and 2.8 m s^{-1} and typical values of gravity wave temperature perturbations of ± 0.6 K (which horizontal wavelengths are similar to the reference Venus LES including the dynamical heating rate).

The convection in the cloud layer at 60° and midnight is stronger in the no-dynamics case. It extends from 1.0×10^5 to 2.5×10^4 Pa (48.0 to 56.4 km). In contrast, at the equator at noon the convection is very weak

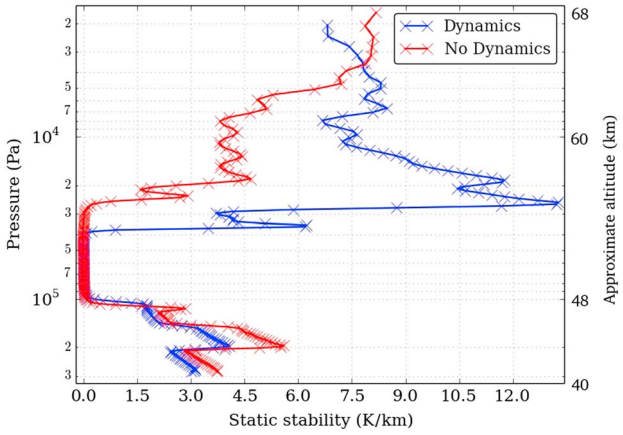

Figure 17. Comparison of the average static stability (K/km) vertical profile with and without dynamics, for equator, midnight.

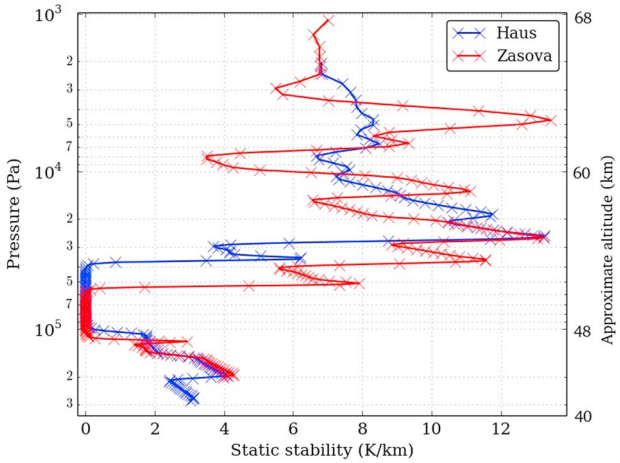

Figure 18. Comparison of the average static stability (K/km) vertical profile at the equator at midnight between forcing using heating rates calculated from *Haus et al.* [2014] and *Zasova et al.* [2007] cloud models.

when the large-scale dynamical heating rate is neglected. At the altitude of 9.0×10^4 Pa, an area with much weaker plumes is visible, with a lack of organization as clear polygonal cells. The variabilities with latitude and local time of the case without dynamics are very similar to the ones of *Imamura et al.* [2014].

Our exploration in this section thus reinforces the conclusion from section 4 that the global dynamics plays a important part in the variability of the convective layer with latitude and local time.

5.2. Cloud Model

In the modeling of the chemical and microphysical processes being a work in progress in the LMD Venus GCM, the formation of clouds is not yet implemented in our simulations: a cloud radiative model is simply derived from the observations. In the results presented so far, the cloud model of *Haus et al.* [2014] was used. To test the sensitivity of our predictions to the cloud model, we carried out Venus LES using heating rates derived from LMD Venus GCM runs with the cloud model of *Zasova et al.* [2007] [see *Lebonnois et al.*, 2016]. Retrievals of the cloud properties in *Haus et al.* [2014] (hereafter H14) are based on VIRTIS/VEX spectra, while *Zasova et al.* [2007] (hereafter Z07) used data set from Venera 15/Venera 16 and Vega 1/Vega 2 missions. In Figure 18 we compare the results of Venus LES using the two distinct cloud models.

The convective layers obtained with the two cloud models clearly exhibit differences, which make the choice of cloud model a key aspect in modeling the convection in the Venusian cloud layer. With the Z07 cloud model, the convection extends from 1.2×10^5 Pa to 5.5×10^4 Pa with vertical wind between -1.7 and 1.7 m s^{-1} and temperature perturbations with typical values of $\pm$ 0.2 K. Hence, the convective layer is both thicker and higher (thus more consistent with the VeRa profiles) when using the H14 cloud model than when using the Z07 model. There is no predicted difference, however, in the wavelengths of the emitted gravity waves and the variability of the cloud layer convection in latitude and local time. This preliminary analysis remains to be complemented in future work coupling our Venus LES model with a representation of microphysical processes as in *McGouldrick and Toon* [2008].

6. Conclusion

We performed unprecedented three-dimensional LES simulations of the convective cloud layer of Venus and the induced gravity waves, with a radiative forcing consisting of IR and solar heating rates and an additional heating rate associated with the global circulation extracted from the LMD Venus GCM.

The resolved convective layer is several kilometers thick, with vertical winds up to several meters per second, and organized horizontally as polygonal closed cells of about 10 km wide. The gravity waves emitted by the convection (both above and below the convective layer) drive temperature perturbations of several tenths of kelvins with vertical wavelengths from 1 to 3 km and horizontal wavelengths from 1 to about 10 km. These results are in good agreement with the observations though our Venus LES is underestimating the thickness of the convective layer and the amplitude of the gravity waves. As expected, the convective layer is strongly

dependent on the cloud model used to calculate the heating rates, with the latest cloud model of *Haus et al.* [2014] providing better comparison with observations.

The variability of the model with latitude and local time is different from previous modeling. The addition of the heating rate associated with the global circulation provides an estimate of the impact of the global circulation on the convective layer and proves to be a crucial inclusion to Venus LES for the cloud layer. By warming up and cooling down the convective layer, the global dynamics tends to mitigate the convection.

The simplicity of the adopted forcing may be responsible for the differences between our model predictions and the observations. Indeed, a complete radiative-photochemical-dynamical coupling in our Venus LES may be key to understand the convective cloud layer of Venus. The follow-up to this work is thus to develop a Venus LES model capable to couple the WRF dynamical integrations with the complete physical parameterizations for Venus by *Lebonnois et al.* [2016], in a broader project to build a complete mesoscale model for Venus in a similar fashion to what was done on Mars by *Spiga and Forget* [2009]. Another area of improvement is to implement an extension of the domain in the vertical (from 0 to about 90 km) to resolve the planetary boundary layer and the two convective layers (18–30 km and 50–60 km altitudes) and in the horizontal over 100 km wide to study the full spectrum of emitted gravity waves, and their possible link with topography [*Blamont et al.*, 1986; *Sagdeyev et al.*, 1992; *Titov et al.*, 2012; *Piccialli et al.*, 2014; *Bertaux et al.*, 2016]. Further applications of our Venus mesoscale model will undoubtedly arise in the near future from the upcoming observations of Akatsuki and future Venus missions.

Acknowledgments
The authors acknowledge support from CNES and thank the two reviewers for their constructive comments which helped to improve the paper. Results from the simulations performed in this paper are available upon request (contact: maxence.lefevre@lmd.jussieu.fr).

References

Agee, E. M., T. S. Chen, and K. E. Dowell (1973), A review of mesoscale cellular convection, *Bull. Am. Meteorol. Soc.*, *54*, 1004–1012, doi:10.1175/1520-0477(1973)054<1004:AROMCC>2.0.CO;2.

Atkinson, B. W., and J. W. Zhang (1996), Mesoscale shallow convection in the atmosphere, *Rev. Geophys.*, *34*, 403–431, doi:10.1029/96RG02623.

Baker, R. D., G. Schubert, and P. W. Jones (1998), Cloud-Level penetrative compressible convection in the Venus atmosphere, *J. Atmos. Sci.*, *55*, 3–18, doi:10.1175/1520-0469(1998)055<0003:CLPCCI>2.0.CO;2.

Baker, R. D., G. Schubert, and P. W. Jones (1999), High Rayleigh number compressible convection in Venus' atmosphere: Penetration, entrainment, and turbulence, *J. Geophys. Res.*, *104*, 3815–3832, doi:10.1029/1998JE900029.

Baker, R. D., G. Schubert, and P. W. Jones (2000a), Convectively generated internal gravity waves in the lower atmosphere of Venus. I: No wind shear, *J. Atmos. Sci.*, *57*, 184–199, doi:10.1175/1520-0469(2000)057<0184:CGIGWI>2.0.CO;2.

Baker, R. D., G. Schubert, and P. W. Jones (2000b), Convectively generated internal gravity waves in the lower atmosphere of Venus. II: Mean wind shear and wave-mean flow interaction, *J. Atmos. Sci.*, *57*, 200–215, doi:10.1175/1520-0469(2000)057<0200:CGIGWI>2.0.CO;2.

Belton, M. J. S., G. R. Smith, G. Schubert, and A. D. del Genio (1976), Cloud patterns, waves and convection in the Venus atmosphere, *J. Atmos. Sci.*, *33*, 1394–1417, doi:10.1175/1520-0469(1976)033<1394:CPWACI>2.0.CO;2.

Bertaux, J.-L., I. V. Khatuntsev, A. Hauchecorne, W. J. Markiewicz, E. Marcq, S. Lebonnois, M. Patsaeva, A. Turin, and A. Fedorova (2016), Influence of Venus topography on the zonal wind and UV albedo at cloud top level: The role of stationary gravity waves, *J. Geophys. Res. Planets*, *121*, 1087–1101, doi:10.1002/2015JE004958.

Blamont, J. E., et al. (1986), Implications of the VEGA balloon results for Venus atmospheric dynamics, *Science*, *231*, 1422–1425, doi:10.1126/science.231.4744.1422.

Counselman, C. C., S. A. Gourevitch, R. W. King, G. B. Loriot, and E. S. Ginsberg (1980), Zonal and meridional circulation of the lower atmosphere of Venus determined by radio interferometry, *J. Geophys. Res.*, *85*, 8026–8030, doi:10.1029/JA085iA13p08026.

Crisp, D. (1986), Radiative forcing of the Venus mesosphere. I—Solar fluxes and heating rates, *Icarus*, *67*, 484–514.

Deardorff, J. W. (1972), Numerical investigation of neutral and unstable planetary boundary layers, *J. Atmos. Sci.*, *29*, 91–115, doi:10.1175/1520-0469(1972)029<0091:NIONAU>2.0.CO;2.

Eymet, V., R. Fournier, J.-L. Dufresne, S. Lebonnois, F. Hourdin, and M. A. Bullock (2009), Net exchange parameterization of thermal infrared radiative transfer in Venus' atmosphere, *J. Geophys. Res.*, *114*, E11008, doi:10.1029/2008JE003276.

Fovell, R., D. Durran, and J. R. Holton (1992), Numerical simulations of convectively generated stratospheric gravity waves, *J. Atmos. Sci.*, *49*, 1427–1442, doi:10.1175/1520-0469(1992)049<1427:NSOCGS>2.0.CO;2.

Frits, D. C., and M. J. Alexander (2003), Gravity wave dynamics and effects in the middle atmosphere, *Rev. Geophys.*, *41*, 1112–1131, doi:10.1029/2001RG000106.

Gierasch, P. J., et al. (1997), The general circulation of the Venus atmosphere: An assessment, in *Venus II: Geology, Geophysics, Atmosphere, and Solar Wind Environment*, edited by J. W. Bucher, D. M. Hunten, and R. J. Phillips, pp. 459–500, Univ. of Ariz. Press, Tucson, Ariz.

Haus, R., D. Kappel, and G. Arnold (2013), Self-consistent retrieval of temperature profiles and cloud structure in the northern hemisphere of Venus using VIRTIS/VEX and PMV/VENERA-15 radiation measurements, *Planet. Space Sci.*, *89*, 77–101, doi:10.1016/j.pss.2013.09.020.

Haus, R., D. Kappel, and G. Arnold (2014), Atmospheric thermal structure and cloud features in the southern hemisphere of Venus as retrieved from VIRTIS/VEX radiation measurements, *Icarus*, *232*, 232–248, doi:10.1016/j.Icarus.2014.01.020.

Hinson, D. P., and J. M. Jenkins (1995), Magellan radio occultation measurements of atmospheric waves on Venus, *Icarus*, *114*, 310–327, doi:10.1006/icar.1995.1064.

Hou, A. Y., and B. F. Farrell (1987), Superrotation induced by critical-level absorption of gravity waves on Venus: An assessment, *J. Atmos. Sci.*, *44*, 1049–1061, doi:10.1175/1520-0469(1987)044<1049:SIBCLA>2.0.CO;2.

Hueso, R., J. Peralta, and A. Sánchez-Lavega (2012), Assessing the long-term variability of Venus winds at cloud level from VIRTIS-Venus Express, *Icarus*, *217*, 585–598, doi:10.1016/j.icarus.2011.04.020.

Hueso, R., J. Peralta, I. Garate-Lopez, T. V. Bandos, and A. Sánchez-Lavega (2015), Six years of Venus winds at the upper cloud level from UV, visible and near infrared observations from VIRTIS on Venus Express, *Planet. Space Sci.*, *113*, 78–99, doi:10.1016/j.pss.2014.12.010.

Imamura, T., T. Higuchi, Y. Maejima, M. Takagi, N. Sugimoto, K. Ikeda, and H. Ando (2014), Inverse insolation dependence of Venus' cloud-level convection, *Icarus*, *228*, 181–188, doi:10.1016/j.Icarus.2013.10.012.

Kerzhanovich, V. V., et al. (1986), Smallscale turbulence in the Venus middle cloud layer, *Sov. Astron. Lett.*, *12*, 20–22.

Khatuntsev, I. V., M. V. Patsaeva, D. V. Titov, N. I. Ignatiev, A. V. Turin, S. S. Limaye, W. J. Markiewicz, M. Almeida, T. Roatsch, and R. Moissl (2013), Cloud level winds from the Venus express monitoring camera imaging, *Icarus*, *226*, 140–158, doi:10.1016/j.icarus.2013.05.018.

Lebonnois, S., F. Hourdin, V. Eymet, A. Crespin, R. Fournier, and F. Forget (2010), Superrotation of Venus' atmosphere analyzed with a full general circulation model, *J. Geophys. Res.*, *115*, E06006, doi:10.1029/2009JE003458.

Lebonnois, S., V. Eymet, C. Lee, and J. Vatant d'Ollone (2015), Analysis of the radiative budget of the Venusian atmosphere based on infrared Net Exchange Rate formalism, *J. Geophys. Res. Planets*, *120*, 1186–1200, doi:10.1002/2015JE004794.

Lebonnois, S., N. Sugimoto, and G. Gilli (2016), Wave analysis in the atmosphere of Venus below 100-km altitude, simulated by the LMD Venus GCM, *Icarus*, *278*, 38–51, doi:10.1016/j.icarus.2016.06.004.

Leroy, S. S., and A. P. Ingersoll (1995), Convective generation of gravity waves in Venus's atmosphere: Gravity wave spectrum and momentum transport, *J. Atmos. Sci.*, *52*, 3717–3737, doi:10.1175/1520-0469(1995)052<3717:CGOGWI>2.0.CO;2.

Lilly, D. K. (1962), On the numerical simulation of buoyant convection, *Tellus*, *14*(2), 148–172.

Linkin, V. M., et al. (1986), VEGA balloon dynamics and vertical winds in the Venus middle cloud region, *Science*, *231*, 1417–1419, doi:10.1126/science.231.4744.1417.

Markiewicz, W. J., D. V. Titov, S. S. Limaye, H. U. Keller, N. Ignatiev, R. Jaumann, N. Thomas, H. Michalik, R. Moissl, and P. Russo (2007), Morphology and dynamics of the upper cloud layer of Venus, *Nature*, *450*, 633–636, doi:10.1038/nature06320.

McGouldrick, K., and O. B. Toon (2008), Observable effects of convection and gravity waves on the Venus condensational cloud, *Planet. Space Sci.*, *56*, 1112–1131, doi:10.1016/j.pss.2008.02.010.

Moeng, C., J. Dudhia, J. Klemp, and P. Sullivan (2007), Examining two-way grid nesting for large Eddy simulation of the PBL using the WRF model, *Mon. Weather Rev.*, *135*(6), 2295–2311.

Peralta, J., R. Hueso, A. Sánchez-Lavega, G. Piccioni, O. Lanciano, and P. Drossart (2008), Characterization of mesoscale gravity waves in the upper and lower clouds of Venus from VEX-VIRTIS images, *J. Geophys. Res.*, *113*, E00B18, doi:10.1029/2008JE003185.

Piccialli, A., D. V. Titov, A. Sánchez-Lavega, J. Peralta, O. Shalygina, W. J. Markiewicz, and H. Svedhem (2014), High latitude gravity waves at the Venus cloud tops as observed by the Venus Monitoring Camera on board Venus Express, *Icarus*, *227*, 94–111, doi:10.1016/j.Icarus.2013.09.012.

Rossow, W. B., A. D. del Genio, S. S. Limaye, and L. D. Travis (1980), Cloud morphology and motions from Pioneer Venus images, *J. Geophys. Res.*, *85*, 8107–8128, doi:10.1029/JA085iA13p08107.

Sagdeev, R. Z., et al. (1986), Overview of VEGA Venus balloon in situ meteorological measurements, *Science*, *231*, 1411–1414, doi:10.1126/science.231.4744.1411.

Sagdeyev, R. Z., et al. (1992), Differential VLBI measurements of the Venus atmosphere dynamics by balloons—VEGA project, *Astron. Astrophys.*, *254*, 387–392.

Sánchez-Lavega, A., et al. (2008), Variable winds on Venus mapped in three dimensions, *Geophys. Res. Lett.*, *35*, L13204, doi:10.1029/2008GL033817.

Schubert, G., and R. L. Walterscheid (1984), Propagation of small-scale acoustic-gravity waves in the Venus atmosphere, *J. Atmos. Sci.*, *41*, 1202–1213, doi:10.1175/1520-0469(1984)041<1202:POSSAG>2.0.CO;2.

Seiff, A., D. B. Kirk, R. E. Young, R. C. Blanchard, J. T. Findlay, G. M. Kelly, and S. C. Sommer (1980), Measurements of thermal structure and thermal contrasts in the atmosphere of Venus and related dynamical observations—Results from the four Pioneer Venus probes, *J. Geophys. Res.*, *85*, 7903–7933, doi:10.1029/JA085iA13p07903.

Skamarock, W. C., and J. B. Klemp (2008), A time-split nonhydrostatic atmospheric model for weather research and forecasting applications, *J. Comput. Phys.*, *227*, 3465–3485.

Spiga, A., and F. Forget (2009), A new model to simulate the Martian mesoscale and microscale atmospheric circulation: Validation and first results, *J. Geophys. Res.*, *114*, E02009, doi:10.1029/2008JE003242.

Spiga, A., F. Forget, S. R. Lewis, and D. P. Hinson (2010), Structure and dynamics of the convective boundary layer on Mars as inferred from large-eddy simulations and remote-sensing measurements, *Q. J. R. Meteorol. Soc.*, *136*, 414–428, doi:10.1002/qj.563.

Sullivan, P. P., and E. G. Patton (2011), The effect of mesh resolution on convective boundary layer statistics and structures generated by large-eddy simulation, *J. Atmos. Sci.*, *68*, 2395–2415, doi:10.1175/JAS-D-10-05010.1.

Svedhem, H., et al. (2007), Venus express—The first European mission to Venus, *Planet. Space Si.*, *55*, 1636–1652, doi:10.1016/j.pss.2007.01.013.

Tellmann, S., B. Haeusler, M. Paetzold, M. K. Bird, G. L. Tyler, T. Andert, and S. Remus (2009), The Structure of the Venus neutral atmosphere as seen by the radio science experiment VeRa on Venus express, *J. Geophys. Res.*, *114*, E00B36, doi:10.1029/2008JE003204.

Tellmann, S., B. Häusler, D. P. Hinson, G. L. Tyler, T. P. Andert, M. K. Bird, T. Imamura, M. Pätzold, and S. Remus (2012), Small-scale temperature fluctuations seen by the VeRa radio science experiment on Venus express, *Icarus*, *221*, 471–480, doi:10.1016/j.Icarus.2012.08.023.

Titov, D. V., et al. (2012), Morphology of the cloud tops as observed by the Venus express monitoring camera, *Icarus*, *217*, 682–701, doi:10.1016/j.icarus.2011.06.020.

Torrence, C., and G. P. Compo (1998), A practical guide to wavelet analysis, *Bull. Am. Meteorol. Soc.*, *79*, 61–78.

VanZandt, T. E., and D. C. Fritts (1989), A theory of enhanced saturation of the gravity wave spectrum due to increases in atmospheric stability, *Pure Appl. Geophys.*, *130*(2), 399–420, doi:10.1007/BF00874466.

Yamamoto, M. (2014), Idealized numerical experiments on microscale eddies in the Venusian cloud layer, *Earth Planets Space*, *66*, 27, doi:10.1186/1880-5981-66-27.

Young, R. E., R. L. Walterscheid, G. Schubert, A. Seiff, V. M. Linkin, and A. N. Lipatov (1987), Characteristics of gravity waves generated by surface topography on Venus—Comparison with the VEGA Balloon results, *J. Atmos. Sci.*, *44*, 2628–2639, doi:10.1175/1520-0469(1987)044<2628:COGWGB>2.0.CO;2.

Zasova, L. V., N. Ignatiev, I. Khatuntsev, and V. Linkin (2007), Structure of the Venus atmosphere, *Planet. Space Sci.*, *55*, 1712–1728, doi:10.1016/j.pss.2007.01.011.